INTERNATIONAL TABLES FOR CRYSTALLOGRAPHY

ISSN 1574-8707
it.iucr.org

Volume I, X-ray Absorption Spectroscopy and Related Techniques
ISBN: 978-1-119-43394-1

Chapter 2.8

Keywords: X-ray fluorescence; X-ray absorption spectroscopy; absorption edges; X-ray scattering; Auger; electron yield.

XAFS with secondary process modalities and introduction to fluorescence and nonradiative processes

Christopher T. Chantler*

School of Physics, University of Melbourne, Victoria 3010, Australia. *Correspondence e-mail: chantler@unimelb.edu.au

This chapter introduces and discusses the origin of X-ray absorption spectroscopy (XAS) in its application to fluorescence detection and related secondary detection modalities. XAS in general is a nascent technology and theory, and exciting applications continue to evolve. Later chapters will develop the theory and applications to old and new experimental fields within the broad umbrella of XAS. Approximations are made in this overview which will be questioned or adapted in later advanced topics.

1. Overview

This chapter looks at modalities for the investigation of X-ray absorption spectroscopy which do not use a transmission geometry. As the most popular, initial and dominant consideration is given to fluorescence measurements, together with alternate geometries, Auger nonradiative processes, secondary modalities and the challenge of identifying common and distinct information content.

We begin (Section 2) with a brief discussion of the importance of fluorescence detection and of all secondary modalities. Section 3 raises the question, and perhaps confusion, of the order of the process of fluorescence as seen in X-ray absorption spectroscopy, whether it be nth-order perturbation theory, kth order in the vector potential or an m-step process. Clarity on this question is important for all secondary modalities, yet their applications can be very distinct.

Concentrating on fluorescence measurements, we then (Section 4) consider the dominant experimental systematic in fluorescence measurements which impairs any approach to directly compare the information content of the technique. Having addressed the basic theory, we investigate the variation of signal and information content with several well established geometries in the literature (Section 5). This variation is quite dramatic.

Section 6 returns to secondary, nonradiative processes and Auger decay. Section 7 continues the discussion of secondary modalities with electron-yield measurements. While there is considerable advice in the literature regarding recommendations for the detection modality for a specific experiment, we find that the regimes of interest and relevant modalities for particular investigations require clarity and redefinition, as presented in Section 8. We present this at two levels: firstly on a level where we hope that advanced scientists and crystallographers may learn new possible applications and approaches, and secondly as a simple guide for those looking for an appropriate incisive technique for their particular sample and scientific question. However, we attempt to avoid being

Related chapters

Volume I: 2.1, 2.9, 2.11, 2.16, 2.19, 2.20, 2.21, 2.25, 3.13, 3.14, 3.31, 3.32

prescriptive or proscriptive as to modality. We conclude with a brief summary and discussion of coming opportunities and point towards other chapters in this volume for further information from this introduction.

1.1. Definitions

XAFS, X-ray absorption fine structure; XANES, X-ray absorption near-edge structure; RoI, region of interest; TDPT: time-dependent perturbation theory; RIXS, resonant inelastic X-ray scattering; $[\mu/\rho]$, (total) mass attenuation coefficient; $[\mu_f/\rho]$, (total) mass attenuation coefficient at a fluorescence energy; $[\mu/\rho]_{pe}$, photoelectric mass absorption coefficient; $[\mu/\rho]^*_{pe}$, photoelectric mass absorption coefficient for the active atom and orbital; $[\rho t]$, density and thickness of sample (integrated column density); $[\mu/\rho]_M$, (total) mass attenuation coefficient of the substrate (matrix, solvent) upon which the sample is deposited or in which the sample is embedded; α, incident angle of the photon on the sample (0 for grazing and $\pi/2$ for normal incidence); β, angle of emission of the scattered photon from the sample.

2. Fluorescence

The basic processes of X-ray interaction with matter are illustrated in Fig. 1. Many of the earlier chapters in this volume have discussed the theory of X-ray absorption spectroscopy in absorption, *i.e.* in the transmission geometry. Fluorescence measurement XAFS, developed by Jaklevic *et al.* (1977), is a particularly useful technique for the structural investigation of highly dilute and inhomogeneous systems (Jaklevic *et al.*, 1993; Lee *et al.*, 1981) and is by far the most commonly used XAS technique in modern experiments.

Fluorescence energies are sharp, discrete and dominated by the characteristic X-radiation. Hence, if photoionization ejects an electron from the inner 1*s* or *K* shell, then the fluorescent radiation is dominated by $K\alpha_1$ and $K\alpha_2$, with some lesser contribution from $K\beta_{13}$ if the $n = 3$ shells are populated, for higher atomic number Z. Hence, fluorescence can be seen as

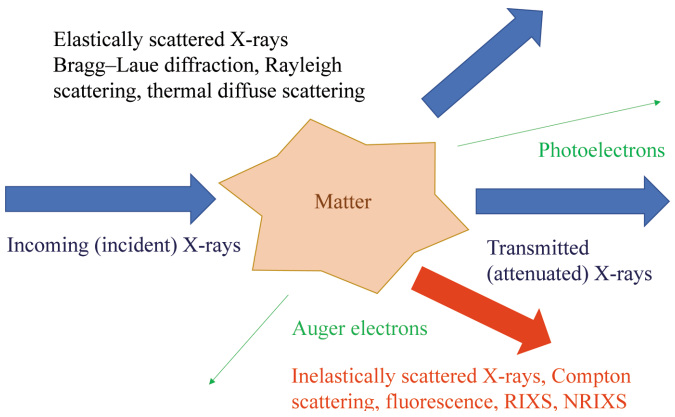

Figure 1
Basic processes in the interaction of X-rays with matter. Discussed in detail in Volume C of *International Tables for Crystallography* and in Chantler & Creagh (2024).

one of the possible consequences of photoionization, as one of the relaxation processes, with a delay time corresponding to the excited-state lifetime. Nonradiative decay commonly leads to secondary Auger electron emission with a low electron energy. As a user the question of the order of fluorescence might seem irrelevant, but it is of course crucial to the understanding and implementation of the theory of XAS and dictates the insight, information depth and information content which can be extracted from a particular experiment.

3. The problem of order of perturbation theory, process timescales and information content

Quantum mechanics often refers to two-step or multiple-order processes. A two-step process is a physical process where the first step is 'complete' before the second one commences; that is, the steps are at least approximately separable and time-ordered. A process can be denoted as first order if it is a first-order contribution in perturbation theory or first order in the Hamiltonian. All physical processes depend upon the time-dependence of the Hamiltonian and time-dependent perturbation theory (TDPT). A process can be first order in the vector potential **A** if the (perturbing) term in the Hamiltonian causing the process is linear in **A**. If, for example, a process is third order in $\mathbf{A}^2$ or third order in that component of the Hamiltonian, it will be a third-order TDPT process and a sixth-order process in **A**.

Absorption is a one-step process, whether a bound–bound excitation or ionization to the continuum is involved. Similarly, relaxation by fluorescence (the emission of a fluorescent or characteristic radiation photon) is a one-step process which could arise from absorption or recombination. However, absorption (ionization) followed by fluorescence is a two-step process if the two are time-ordered and separable.

Therefore fluorescence is seen as a two-step or second-order process, including photoionization or photoexcitation. The first step leaves the atom or quantum system in an excited state, with a hole, for example in the *K* shell, and the secondary process de-excites the excited-state system by filling the subshell hole with an outer-shell electron (for example from the *L* shell, either $K\alpha_1$ if the electron relaxes from the $2p_{3/2}$ subshell or $K\alpha_2$ if the electron relaxes from the $2p_{1/2}$ subshell). This gives rise to a fluorescent photon and characteristic radiation (*i.e.* $K\alpha_1$, $K\alpha_2$, $K\beta_{13}$, $L\alpha_1$ *et seq.*).

If photoionization displays all the oscillations of XAFS as a function of k or E, due to the photoelectron interference wave from elastic electron scattering modulating the mass absorption coefficient or cross section, then any consequent, causal secondary process must display the same oscillation of probability. Hence, when true, the core information content of fluorescence detection (of photoionization and XAFS) should be identical to that of transmission or absorption XAFS. This potential synergy and identity led to the development of fluorescence XAFS by Jaklevic *et al.* (1977), which has now become the mainstay of XAFS structural analysis.

The same argument does not generally apply to the pre-edge structure, which will non-uniformly populate or

Table 1
Selection rules for multipole transitions.

Process	Width	Lifetime
Absorption	Electric dipole allowed $E1$	$\tau \simeq 1/A \simeq 10^{-20}$ s
Relaxation	$\Gamma < 0.001$ eV for $Z = 1$, increasing to typically 125 eV for high Z	$\tau = 27.2/[\Gamma(4.13414 \times 10^{16})]$ s $\simeq 6.6 \times 10^{-16}/\Gamma$ s
XAFS interference	Electron IMFP 1–30 Å, $v = (2E_e/m_e)^{1/2} = \hbar k/m_e$; $v \simeq 5.93 \times 10^5 (E_e)^{1/2}$ $\simeq 1.16 \times 10^6 k$ m s^{-1}	$\tau \simeq 1$–$30 \times 10^{-16}/k$ s
Thermal motion		$\tau \simeq 10^{-11}$–10^{-14} s
First-row transition-metal K edge		
Absorption	$E1$	$\tau \simeq 1/A \simeq 10^{-20}$ s
Relaxation	$\Gamma \simeq 1$ eV	$\tau = 27.2/[\Gamma(4.13414 \times 10^{16})]$ s $\simeq 6.6 \times 10^{-16}/\Gamma$ s
XAFS interference	$k \simeq 20$ Å^{-1}; $v \simeq 5.93 \times 10^5 (E_e)^{1/2} \simeq 1.16 \times 10^6 k$ m s^{-1}	$\tau \simeq 0.5$–15×10^{-17} s
Medium-Z L_1 edge (Coster–Kronig dominated)		
Absorption	$E1$	$\tau \simeq 1/A \simeq 10^{-20}$ s
Relaxation	$\Gamma \simeq 0$–20 eV	$\tau = 27.2/[\Gamma(4.13414 \times 10^{16})]$ s $\simeq 6.6 \times 10^{-16}/\Gamma$ s
XAFS interference	$k \simeq 20$ Å^{-1}; $v \simeq 5.93 \times 10^5 (E_e)^{1/2} \simeq 1.16 \times 10^6 k$ m s^{-1}	$\tau \simeq 0.5$–15×10^{-17} s

depopulate those upper states which would lead to the corresponding fluorescence spectra. Hence, the pre-edge region in XANES may be strongly damped or modulated in fluorescence detection compared with transmission measurements, and this should be carefully understood in comparing spectra and structure, especially with a limited or variable RoI (region of interest), but also in the case of full-spectrum data collection and processing.

As discussed in Chantler & Creagh (2024), photoionization is a first-order process dominated by the $\mathbf{A} \cdot \mathbf{p}$ term in the Hamiltonian. However, the XAFS and XANES interference term depends upon an elastically scattered electron interference wave and contributions from multiple scattering *etc.*, and this arises from the second- and higher-order processes with a timescale corresponding to the photoelectron wave velocity or momentum and the range at which scattering occurs. Each of these electron-scattering events must involve a time-dependent component of the Hamiltonian and corresponding propagator, and they are usually not able to be time-ordered, so they represent high-order processes intrinsic to the observation of XAFS and XANES.

For fluorescence or any other secondary process to yield the same signature and structural information as transmission XAFS, the scattering time should be less than the decay or relaxation time. Different timescales arise in the overall scattering process (Table 1).

The hole widths for relaxation of typically $\Gamma < 0.001$ eV for $Z = 1$, increasing to typically 125 eV for high Z, correspond to lifetimes of $\tau = 27.2/[\Gamma(4.13414 \times 10^{16})]$ s $\simeq 6.6 \times 10^{-16}$ s/Γ. By contrast, the absorption rate corresponds to a time constant for photon absorption of the order of $\tau = 1/A \simeq 10^{-20}$ s for electric dipole-allowed processes and thus is generally very fast compared with the relaxation (Joly & Grenier, 2016).

For XAFS interference timescales, the electron inelastic mean free path is typically 1–30 Å and the velocity of the photoelectron $v = (2E_e/m_e)^{1/2} = \hbar/m_e$, where $m_e = 9.10938356 \times 10^{-31}$ kg and $\hbar = 1.0545718 \times 10^{-34}$ m^2 kg s^{-1}, so $v \simeq 5.93 \times 10^5 (E_e)^{1/2} \simeq 1.16 \times 10^6 k$ m s^{-1} with E_e in eV and k in Å^{-1}. Therefore, the XAFS interference time is typically 1–30 $\times 10^{-16}/k$ s.

Thermal motion of nuclei, electric potential and molecules is generally very slow. Hence, the timescale associated with thermal nuclear motion typically varies from 10^{-11} to 10^{-14} s, so that the XAFS interference and relaxation can be seen as measuring a frozen snapshot of any thermal motion or distribution. More carefully, the Franck–Condon principle defines the expectation value of transition energies between lower and excited states based upon the thermal or wavefunction radial distribution and the relevant transition energies accordingly.

Hence, for medium and high wavevector k and the transition-metal K edge, where $\Gamma \simeq 1$ eV, the XAFS structure is well defined and well within the period of hole relaxation, so that the fluorescence and absorption spectra should be structurally very similar. However, when for example the edge width is dominated by Coster–Kronig transitions (see below) and is large, say 10–20 eV for an L_1 edge, then the ability to separate the two-step process is limited and the structure of XAFS/XANES can be both complex and limited. The width becomes significantly energy-dependent, and the fluorescence process must then be treated as a higher-order perturbative process, with the scattering or ionization treated as part of the fluorescence process. See, in particular, Chantler & Bourke (2024) for hole widths, decay lifetimes, fluorescence yields and inelastic mean free paths, and hence for the scaling of these processes. Also see, for example, Crasemann (1996).

Hence, fluorescence can be seen as a third-order or much higher-order process to reflect the XAFS structure from the electron–atom scattering interaction, especially on the threshold, or a two-step process when XAFS interference is clearly completed prior to the de-excitation and fluorescent characteristic radiation emission, such as for higher energies and EXAFS. For the purposes of measurement, X-ray energies and in particular X-ray characteristic energies and spectra are detailed in Chantler *et al.* (2024). With respect to fluorescence XAFS, it is sufficient to have an experimental RoI or bandpass which covers the range of the relevant spectrum of the fluorescent characteristic transition. This is then a partial fluorescence yield (PFY) measurement, which is normally distinguished by setting an RoI on the photon energy in the solid-state fluorescence detector. In turn, this fluorescence measurement is a natural and important part of the suite of possible measurements of X-ray emission spectroscopy (XES), which includes resonant inelastic X-ray scattering

(RIXS) planes of incident energy and energy transfer, and high energy resolution fluorescence detection (HERFD) collected at a slice in the RIXS plane, for example, and XES measurements of the elastic scattering, to name a few which will be discussed in other chapters in this volume.

There is currently some exciting discussion about the consistency of information from different detection modalities. For example, we have just described conditions under which the information content and range of interference oscillation in transmission XAFS should be similar or identical to that in fluorescence and other modalities. Of course, probes can separate absorption or transmission with different incident synchrotron X-ray polarizations, or characterize fluorescence or electron-yield experiments with different secondary scattering polarities, scattering angles, polarization, RIXS vectors *etc*. These will provide additional or different content compared with the integrated average such as might be obtained in a typical transmission experiment.

Conversely, it should already be clear that the pre-edge structure must be different between transmission measurements and fluorescent measurements, yielding different sensitivity and diagnostic information content. Chantler & Creagh (2024) explain that the transmission spectra from, for example, *K*-edge XAFS and $L_{\rm I}$-edge XAFS should in some sense be consistent with and equivalent to one another, because these spectra are dominated by *s*–*p* dipole operators for the absorption spectra. Conversely, the transmission $L_{\rm II}$ and $L_{\rm III}$ edges should be qualitatively different from the *K*-edge spectra because they involve *p*–*d* or *p*–*s* operators in dominant dipole contributions. Therefore, fluorescence detection using the $K\alpha$ spectra should be most consistent with that of transmission *K*-edge spectra. The use of fluorescence detection based on other spectral components may involve potentially significant contributions from filling 2*p* holes, yielding significant contributions from *d*-orbital or *s*-orbital occupied states. We direct the reader on these points to Chantler & Creagh (2024) and other chapters in this volume where this is explained more fully.

To assess the detailed context of a particular sample system and detection method goes beyond this chapter, and the reader should look at the wide range of exemplars in later parts of this volume. However, here we have the opportunity to explain the logic and advantages of the standard fluorescence detection geometry.

4. The self-absorption functional in fluorescence

X-ray absorption for transmission measurements is given by the Beer–Lambert equation,

$$I_{\rm transmitted} = I_0 \exp\{-[\mu/\rho][\rho t]\}, \qquad (1)$$

where I_0 is the intensity of the incident X-ray beam, $[\mu/\rho]$ is the mass attenuation coefficient of the absorbing material, ρ is the density of the material and t is the thickness of the material. Self-absorption and absorption effects in fluorescence detection were observed early in the development of fluorescence-yield detection of XAS (Goulon *et al.*, 1982). A dramatic discrepancy is seen between raw spectra from transmission and raw spectra from fluorescence measurements. There is a large dispersion between the individual fluorescence pixel spectra and the spectral shape is distorted, impairing high-accuracy analysis. This is particularly due to the self-absorption systematic and uncalibrated detector efficiencies in fluorescence.

The first studies to attempt to correct for self-absorption in fluorescence detection of XAFS were reported by Tröger *et al.* (1992). Previous investigations of these distortions in fluorescence XAFS spectra required knowledge of the sample stoichiometry (Tröger *et al.*, 1992) or of the energy dependence of the absorption coefficients (Pfalzer *et al.*, 1999) or a series of measurements at multiple angles (Eisebitt *et al.*, 1993), and assumed that the effect of the XAFS on the correction term was negligible and that the samples are in the thick limit (Booth & Bridges, 2005). Other issues include the need to consider the beam path for the incident and fluorescent photons, the use of absorption coefficients where attenuation coefficients are needed (Chantler, Rae *et al.*, 2012) and the need to relate the analysis to the observed or measured $[\mu/\rho][\rho t]$ rather than a spline-distorted χ. The derivations of Chantler, Rae *et al.* (2012) and Trevorah *et al.* (2019) are suitable for application to fluorescence-detection experimental XAFS data (see Pfalzer *et al.*, 1999; Bunker, 2010; Tröger *et al.*, 1992). Self-absorption has been discussed in numerous papers, but the necessary information to transform a fluorescence spectrum into a transmission spectrum and thus into a functional linear in the absorption coefficient is presented here,

$$I_{\rm f} = \frac{f I_0 \Omega [\mu/\rho]^*_{\rm pe}/(4\pi\cos\theta_{\rm inc})}{[\mu/\rho]/(\cos\theta_{\rm inc}) + [\mu_{\rm f}/\rho]/(\cos\theta_{\rm out})} \times \left\{1 - \exp\left[-\frac{[\mu/\rho][\rho t]}{\cos\theta_{\rm inc}} - \frac{[\mu_{\rm f}/\rho][\rho t]}{\cos\theta_{\rm out}}\right]\right\}, \qquad (2)$$

where I_0 and ρ are as defined in equation (1), $I_{\rm f}$ is the total number of fluorescence photons produced, the asterisk indicates that only the component absorbed in the active centre producing a fluorescent photon is relevant, 'pe' signifies that only the photoelectric absorption is relevant, f is the fluorescence yield, usually for the specific fluorescence spectrum given by the RoI (for example $K\alpha$ fluorescence), t represents the photon penetration depth into the material, Ω represents the solid angle subtended by each detector pixel, $\theta_{\rm inc}$ is the incident angle of the X-rays onto the sample relative to the normal, $\theta_{\rm out}$ is the angle of emission of the fluorescent radiation from the sample relative to the normal and $[\mu_{\rm f}/\rho]$ represents the mass attenuation coefficient of the material at the energy of the fluorescent photon.

Since each detector pixel represents a different $\theta_{\rm out}$ from the sample surface, there will be a different self-absorption functional for each pixel. This is not simply an overall scaling factor as used by some simpler models, but an energy-dependent functional since $[\mu/\rho]$ is a function of energy. To correct for the upstream attenuation A, we provide the functional

$$\left(\frac{I_{\rm f}}{I_{0\,\rm monitor}}\right)\Big|_A = \frac{I_{\rm f}}{I_0}\left[\frac{1}{\varepsilon_{\rm mon}(E)}\right]_A \exp\left[-\left(\frac{\{[\mu/\rho][\rho t]\}_{\rm air}}{\cos\theta_{\rm air}}\right)_A - \left(\frac{\{[\mu/\rho][\rho t]\}_w}{\cos\theta_w}\right)_A - \left(\frac{\{[\mu/\rho][\rho t]\}_m}{\cos\theta_m}\right)_A - \left(\frac{\{[\mu/\rho][\rho t]\}_c}{\cos\theta_c}\right)_A\right], \quad (3)$$

where $I_{\rm f}$ and I_0 are as defined in equation (2), ε represents the overall quantum efficiency of the detectors (as discussed), $\theta_{\rm air}$ represents the incident angle of the radiation to the air (always perpendicular) and $t_{\rm air}/\cos\theta_{\rm air}$ represents the path length that the photons took through air between the sample surface and the front face of the detector, and similarly for any window materials w, the monitor gas path m and the cryostat or other gas c. A common setup uses silicone adhesive on Kapton windows, for example. The subscript A indicates that this equation describes absorption (transmission) components using the incident synchrotron spectral distribution. The $[\mu/\rho]$ terms represent the mass attenuation coefficient of each material and are functions of energy. The experimental thicknesses and densities should be measured to a good accuracy if this is to be calibrated (Chantler *et al.*, 2015).

Signal is lost due to attenuation through the air path, the Kapton (polyimide) tape, detector windows and other materials in the experimental setup. If the X-ray photons pass through a certain thickness of any particular medium, then some fraction of them will be attenuated and not reach the detector.

A second functional is required to account for fluorescent photons emitted from the sample surface. In 'transmission mode' all experimental components are exposed to some fraction of the incident radiation from the synchrotron source. Thus, all experimental components will be exposed to the monochromatic source radiation at whatever energy is being produced by the source. Whilst a transmission experimental setup is arranged in a linear fashion, and a significant amount of radiation is transmitted through the sample, by contrast in 'fluorescence mode' all experimental components downstream from the sample are arranged at a detection angle, for example perpendicularly to the path of the incident source radiation.

We discuss different geometries below, but the key reasons for an approximately perpendicular detection for fluorescence are (i) the penetration depth into the sample is greatest, so that the measurement relates most closely to bulk properties of the sample, (ii) one achieves zero elastic scattering of the in-plane polarization, so that elastically scattered radiation will be polarized, (iii) inelastically scattered radiation shows a peak in intensity in this region and (iv) fluorescent photons as a two-step process will be intrinsically isotropic so that the detection angle is not so critical, yet it is therefore well separated from elastic scattering and forward transmission, and this can have quite a clean background and therefore good signal to noise.

Hence, components downstream from the sample are only exposed to radiation at specific fluorescence energies. This means that equation (3) applies to upstream components similarly for both transmission and fluorescence, with a second functional considering elements downstream of the sample that are only exposed to fluorescence radiation (equation 4),

$$\left(\frac{I_{\rm f\,detected}}{I_{0\,\rm monitor}}\right)\Big|_{\rm measured} = \left(\frac{I_{\rm f}}{I_{0\,\rm monitor}}\right)\Big|_A \left[\varepsilon_{\rm det}(E_{\rm f})\right]_F \times \exp\left[-\left(\frac{\{[\mu_f/\rho][\rho t]\}_{\rm air}}{\cos\theta_{\rm air}}\right)_F - \left(\frac{\{[\mu_{\rm f}/\rho][\rho t]\}_w}{\cos\theta_w}\right)_F - \left(\frac{\{[\mu_{\rm f}/\rho][\rho t]\}_m}{\cos\theta_m}\right)_F - \left(\frac{\{[\mu_{\rm f}/\rho][\rho t]\}_c}{\cos\theta_c}\right)_F\right], \quad (4)$$

where the previous symbols have the same definitions. $(\mu_{\rm f}/\rho)$ represents the mass attenuation coefficient at the energy of the, for example, $K\alpha$ fluorescence photon, and F indicates that this equation describes fluorescence, *i.e.* downstream interactions towards an arbitrary fluorescence detector, where the spectral distribution is given by the fluorescence spectrum, subject to the detection RoI.

Equation (4) is not a function of energy [unlike equation (3) *per se*] but is a function of geometry, source and angle, and hence pixel or detector element. In equation (3) all values of θ are constant (for example 0° or 45° plus offsets accounting for experimental alignment). This is not the case for equation (4) since the downstream fluorescence detector typically has many pixels, each of which is at a different vertical or horizontal relative angular offset. Ideally, the centre of the detector is aligned to be, for example, 90° relative to the path of monochromatic source radiation. The different angular offset for each pixel results in a different path-length term $t/\cos\theta$ and hence a different self-absorption factor for each pixel. There is a symmetry of response for pixels above and below the central line, but in general each pixel has a different correction factor.

More details, to be discussed in the subsequent experimental chapters, include the following.

(i) The chosen fluorescence peak (for example $f_{K\alpha}$, $f_{K\beta}$ or $f_{L\alpha}$) should be indicated by the partial fluorescence yield rather than some nominal total fluorescence yield f. A spectral distribution of incident radiation would lead to a local integral of equation (3), including over a bandpass or divergence, for example, and similarly a spectral distribution of fluorescent radiation would lead to a local integral of, for example, equation (4), including over a spot size and angular distribution on the sample. The local integrals, however, appear to be unnecessary for high accuracy on a number of beamlines, since the functional varies sufficiently slowly and the spot size and divergence are sufficiently small.

(ii) A correction for dead time is assumed to be correct to a high level and without significant error, although if there are wide variations in count rate this would affect the effective efficiency of a pixel unless corrected for in the usual manner.

(iii) The set RoIs (upper and lower level discriminators), which are typical of most fluorescence measurements in most XAS and other applications, ideally exclude any matrix

absorption and scattering, elastic scattering peaks, any non-active atoms in the molecule or solid and any background attenuation from other orbitals. Similarly, it can exclude the pre-edge if the RoI is not well set or if the upper and lower states are not occupied and unoccupied, respectively. The measurement can cross-collect some of the elastic scattering peak plus the small Compton scattering shoulder captured within the RoI window, which depends on the width of this peak, the angle and the RoI, and thus in principle varies between pixels. Most older detectors and beamline collection stations define an RoI and hence cannot correct for this. Some newer full-spectrum analysis can fully exclude these contributions. In general, the overall detector efficiency ratio for each element (equation 3), $[\varepsilon_{\rm det}(E_{\rm f})/\varepsilon_{\rm mon}(E)]$, includes variations of the inelastic peak and shape with scattering angle and how well the detector pixel RoIs are set up for each channel, including whether the RoIs include significant but varying percentage contributions from the fraction of characteristic $K\beta$ radiation, assuming that the RoI was set for the $K\alpha$ fluorescence.

(iv) In fluorescence, the y-axis scale becomes either $a_i[\mu/\rho]^*_{\rm pe}[\rho t]$ or $[\mu/\rho]^*_{\rm pe}[\rho t_{\rm effective}]$. Because of the relative efficiencies of the detectors and any uncertainty in the solid angle and sample depth, this scale cannot have the same meaning as in transmission measurements. In the one-particle approximation, neglecting shake *etc.*, the measured fluorescence signal is $[\mu/\rho]^*_{\rm pe}$. This contrasts with transmission measurements, which include all attenuation processes from active orbitals, background orbitals, inactive atoms in the molecule or solid and any matrix $[\mu/\rho]$. In transmission, the mass attenuation coefficient can be determined on an absolute scale directly interpretable from the full integrated column density $[\rho t]$ of the sample; in fluorescence, this relates at best to some effective depth and so, while hopefully linear and proportional, it is a scaled relative measurement. Hence, fluorescence measurements in general can measure XAFS but cannot (directly) measure absorption or attenuation coefficients on an absolute basis. As a rough approximation, one might interpret a $t_{\rm effective}$ scaling as a $1/e$ depth, which will be energy-dependent but roughly

$$t_{\rm effective} \simeq \frac{1}{\rho[\mu/\rho]_{E,\rm tot} + \rho[\mu/\rho]_{F,\rm tot}},$$

corresponding to the total attenuation of the incident and fluorescent fluxes. This is certainly a functional of pixel angle. This processing allows the interpretation of fluorescence measurements, extracted structure and fitted parameters to be considered on the same basis as the transmission structure, *i.e.* towards χ versus k structure.

5. The challenge of the inverse problem

To extract a theoretical $[\mu/\rho]^*_{\rm pe}$ or χ from a fluorescence measurement, one must invert the above equations. We look at the final observed, measured $(I_{\rm f\,detector}/I_{0\,\rm monitor})|_{\rm measured}$ from equations (2), (3) and (4):

$$\begin{aligned}\left(\frac{I_{\rm f}}{I_0}\right)\Big|_{\rm corrected} = {} & \left(\frac{I_{\rm f\,detector}}{I_{0\,\rm monitor}}\right)\Big|_{\rm measured} \times \left[\frac{\varepsilon_{\rm mon}(E)}{\varepsilon_{\rm det}(E_{\rm f})}\right] \times \frac{4\pi}{f\Omega} \Big/ \\ & \left\{ \exp\left[-\left(\frac{\{[\mu_{\rm f}/\rho][\rho t]\}_{\rm air}}{\cos\theta_{\rm air}}\right)_F - \left(\frac{\{[\mu_{\rm f}/\rho][\rho t]\}_w}{\cos\theta_w}\right)_F \right.\right. \\ & \left.\left. - \left(\frac{\{[\mu_{\rm f}/\rho][\rho t]\}_m}{\cos\theta_m}\right)_F - \left(\frac{\{[\mu_{\rm f}/\rho][\rho t]\}_c}{\cos\theta_c}\right)_F \right\} \Big/ \\ & \left\{ \exp\left[-\left(\frac{\{[\mu/\rho][\rho t]\}_{\rm air}}{\cos\theta_{\rm air}}\right)_A - \left(\frac{\{[\mu/\rho][\rho t]\}_w}{\cos\theta_w}\right)_A \right.\right. \\ & \left.\left. - \left(\frac{\{[\mu/\rho][\rho t]\}_m}{\cos\theta_m}\right)_A - \left(\frac{\{[\mu/\rho][\rho t]\}_c}{\cos\theta_c}\right)_A \right] \right\}, \end{aligned} \tag{5}$$

$$\begin{aligned}\left(\frac{I_{\rm f}}{I_0}\right)\Big|_{\rm corrected} = {} & \frac{\dfrac{[\mu/\rho]^*_{\rm pe}}{\cos\theta_{\rm inc}}}{\dfrac{[\mu/\rho]}{\cos\theta_{\rm inc}} + \dfrac{[\mu_f/\rho]}{\cos\theta_{\rm out}}} \\ & \times \left\{ 1 - \exp\left[-\frac{[\mu/\rho][\rho t]}{\cos\theta_{\rm inc}} - \frac{[\mu_{\rm f}/\rho][\rho t]}{\cos\theta_{\rm out}} \right] \right\}. \end{aligned} \tag{6}$$

Most of the terms in equation (5) are defined or measured and are smooth background functions of energy. The detector efficiencies are complex and pixel-dependent and are retained as an array of fitting coefficients. Potential challenges lie in equation (6), as discussed by Booth & Bridges (2005), because $[\mu/\rho]^*_{\rm pe}$ appears as stated in the numerator, but is also included in $[\mu/\rho] = [\mu/\rho]^*_{\rm pe} + [\mu/\rho]^*_{\rm scat} + [\mu/\rho]^\dagger$ in the denominator and in the exponential, where † refers to all other atoms (matrix, solvent *etc.*) and orbitals and * refers to the active electrons in the active orbital. As stated, only the (mass) photoabsorption coefficient for the electrons in the active orbital can lead to fluorescence.

Formally, this implies that the equation is non-invertible, in particular when $[\mu/\rho] \simeq [\mu/\rho]^*_{\rm pe}$ and the oscillations formally cancel, leaving no signature of the XAFS. In almost all cases the equations can be made invertible by iteration. An equation for χ can be made invertible, except that analysis around the world currently uses different definitions of χ both in the abstract and *in operando*, changing the theoretical interpretation and the comparison of the information content compared with transmission experiments or different edges. Equally, the equation can be inverted directly, with convergence in all practical circumstances, directly in $[\mu/\rho]^*_{\rm pe}$, so that the information content can be assessed directly compared with that from other modalities (Trevorah *et al.*, 2019). While we discuss this in detail here for fluorescence the same approach should apply to all modalities, and especially to alternate experimental fluorescence geometries.

6. Variation of fluorescence theory and information content with geometry

Newville (2014), Bunker (2010) and others note two particularly useful limits for the understanding of fluorescence measurements. In the thin-sample limit, where $[\mu/\rho][\rho t] \ll 1$, the $1 - \exp(X)$ term expands by Taylor series expansion,

cancelling the denominator to first order (and the self-absorption correction) so that equation (2) becomes

$$I_{\rm f} = \frac{fI_0\Omega[\mu/\rho]^*_{\rm pe}[\rho t]}{4\pi\cos\theta_{\rm inc}}. \tag{7}$$

The remainder of equations (3) and (4) remain valid, so that under some ideals we can have

$$[\mu/\rho]^*_{\rm pe} = \left(\frac{I_{\rm f}}{I_0}\right)\bigg|_{\rm corrected} \frac{\cos\theta_{\rm inc}}{[\rho t]} \tag{8}$$

or an approximate equation

$$\left(\frac{I_{\rm f\,detected}}{I_{0\,\rm monitor}}\right)\bigg|_{\rm measured} \simeq \frac{f\Omega[\mu/\rho]^*_{\rm pe}[\rho t]}{4\pi\cos\theta_{\rm inc}}\frac{\varepsilon_{\rm det}(E_{\rm f})}{\varepsilon_{\rm mon}(E)} \times \exp\left[-\frac{[\mu_{\rm f}/\rho]_{\rm air}[\rho t_{\rm air}] + (\mu_{\rm f}/\rho)_w[\rho t_w]}{\cos(\theta_{\rm out,h}-45^\circ)\cos\theta_{\rm out,v}}\right] \tag{9}$$

and to first order the observed intensity ratios are proportional to the photoelectric coefficient and the XAFS structure may be cleanly extracted as a relative measurement. However, this thin-sample limit is invalid whenever a dispersion between detector elements is observed; that is, whenever a fluorescence spectrum for one pixel differs from that for another pixel, or whenever the slope with k is flat or increasing, or whenever it is decreasing but not at the rate corresponding to a transmission measurement, *i.e.* almost always. In these other, common sets of measurement, the functional is nonlinear in $[\mu/\rho]^*_{\rm pe}$.

The second convenient limit is the thick, dilute sample limit where $[\mu/\rho][\rho t] \gg 1$, so the exponential goes to zero, but $[\mu/\rho]_{\rm pe} \ll [\mu/\rho]$, and equation (2) becomes

$$I_{\rm f} = \frac{fI_0\Omega[\mu/\rho]^*_{\rm pe}/(4\pi\cos\theta_{\rm inc})}{[\mu/\rho]/(\cos\theta_{\rm inc}) + (\mu_{\rm f}/\rho)/(\cos\theta_{\rm out})}. \tag{10}$$

The remainder of equations (3) and (4) remain valid so that

$$\left(\frac{I_{\rm f}}{I_0}\right)\bigg|_{\rm corrected} = \frac{[\mu/\rho]^*_{\rm pe}}{\{[\mu/\rho]^*_{\rm pe} + [\mu/\rho]^*_{\rm scat} + [\mu/\rho]^\dagger\} + (\mu_{\rm f}/\rho)\times(\cos\theta_{\rm inc})/(\cos\theta_{\rm out})}; \tag{11}$$

under some ideals, we can have an approximate equation

$$\left(\frac{I_{\rm f\,detected}}{I_{0\,\rm monitor}}\right)\bigg|_{\rm measured} \simeq \frac{\dfrac{f\Omega[\mu/\rho]^*_{\rm pe}}{4\pi\cos\theta_{\rm inc}}}{\dfrac{[\mu/\rho]}{\cos\theta_{\rm inc}} + \dfrac{[\mu_{\rm f}/\rho]}{\cos\theta_{\rm out}}}\frac{\varepsilon_{\rm det}(E_{\rm f})}{\varepsilon_{\rm mon}(E)} \times \exp\left[-\frac{[\mu_{\rm f}/\rho]_{\rm air}[\rho t_{\rm air}] + [\mu_{\rm f}/\rho]_w[\rho t_w]}{\cos(\theta_{\rm out,h}-45^\circ)\cos(\theta_{\rm out,v})}\right]. \tag{12}$$

If, and only if, the angular and energy dependence of the denominator is small, dominated by scattering coefficients or matrix or background absorption, then to first order the observed intensity ratios are proportional to the photoelectric coefficient and the XAFS structure may be cleanly extracted as a relative measurement. However, this limit is also largely independent of fluorescent pixel and angle, so that almost any functional dependence of the slope or spectrum on pixels implies that this limit is not valid. For any pure or concentrated sample, for most of the X-ray regime $[\mu/\rho]_{\rm pe}$ is dominant and is not dominated by the scattering coefficients. The latter only becomes plausible in a dilute disordered solution with a strong matrix, and indeed is not valid at least above millimolar concentrations or above ∼100 p.p.m.. For a typical metallic XAFS investigation, the concentration must be very low for $[\mu/\rho]^*_{\rm pe}$ of the active fluorescent centre in the sample to be dominated by the background absorption $[\mu/\rho]_{\rm pe}$. Then, of course, the signal and statistical precision are also very low. Hence, while both extreme limits are used in conventional analysis of fluorescence XAFS, in most cases the limiting forms are unrealistic or infeasible, and one should use the full analytic form to justify a derivation or relate to theoretical treatments (Chantler, Rae *et al.*, 2012; Newville, 2014; Bunker, 2010).

Three particular geometries alternative to the standard 45° incident and 45° emission angles have been proposed with various advantages over the standard setup. Like transmission measurements, the standard geometry is primarily a bulk-sample measurement, and so the spectra should allow extraction of the bulk absorption spectra and the bulk χ versus k. The 'normal incidence' setup has $\theta_{\rm inc} \simeq$ 1–5° and $\theta_{\rm out} \simeq 90^\circ - (1\text{–}5)^\circ$. In this case the signal is strongly dampened by self-absorption and the dispersion with the detection angle is extremely large, but for a fixed emission angle (pixel) the denominator in equation (2) is largely a constant, so that the spectrum is close to proportional to $[\mu/\rho]^*_{\rm pe}$ (Pease *et al.*, 1989). The technique generally has low efficiency and a small solid angle of detection (Bunker, 2010). As a grazing emission technique, it is a surface probe of the (quantum-mechanical, electronic) density of states (Frenkel *et al.*, 2007) and the information depth is very low, of the order of 10–100 nm, generally approximated as

$$\lambda = 1\Big/\left[\frac{[\mu/\rho]\rho}{\cos\theta_{\rm inc}} + \frac{[\mu_{\rm f}/\rho]\rho}{\cos\theta_{\rm out}}\right] \simeq \frac{\cos\theta_{\rm out}}{[\mu_{\rm f}/\rho]\rho}. \tag{13}$$

Similarly, the 'grazing-incidence' setup has $\theta_{\rm inc} \simeq 90^\circ - (1\text{–}5)^\circ$ and $\theta_{\rm out} \simeq$ (1–5)°. In this case the signal is strongly dampened by absorption and the dispersion with the detection angle is small, but for a fixed emission angle (pixel) the denominator in equation (2) is a strong function of energy, so that the spectrum is close to proportional to $([\mu/\rho]^*_{\rm pe})/[\mu/\rho]$. Hence, the spectrum is strongly distorted in shape and amplitude as a function of E or k (Zschech *et al.*, 1992). As a grazing technique, it is a surface probe of the density of states, and the information depth is very low, of the order of 10–100 nm, generally approximated as

$$\lambda = 1\Big/\left[\frac{[\mu/\rho]\rho}{\cos\theta_{\rm inc}} + \frac{[\mu_{\rm f}/\rho]\rho}{\cos\theta_{\rm out}}\right] \simeq \frac{\cos\theta_{\rm inc}}{[\mu/\rho]\rho}. \tag{14}$$

Similarly, the 'glancing-angle' or 'ReflEXAFS' setup has $90^\circ - \theta_{\rm inc} \simeq 90^\circ - \theta_{\rm out} \simeq$ 2–7 mrad ≃ 0.1–0.5° (Parratt, 1954;

Barchewitz *et al.*, 1978; Martens & Rabe, 1980; Heald *et al.*, 1988; Chen & Heald, 1993). In this case the measurement may be made below the critical angle, in reflectivity, observing the elastic scattering peak in energy in reflection, according to the detector RoI. This is often compared with a corresponding fluorescence measurement measuring the inelastically scattered fluorescence radiation after the 'grazing-incidence' setup. Both signals are heavily distorted by anomalous dispersion and, for example, near-critical angle refractive indices and scattering, but these can be corrected for. The fluorescence signal generally offers greater sensitivity, signal to noise and less distortion of the spectrum, but the reflectivity signal may sometimes be easier to obtain. The reflectivity and fluorescence signals are very sensitive to the geometry and angle. Within certain approximations, simple procedures can obtain $\mu_i(E)$ from the reflectivity curve $R(E)$ (Borthen & Strehblow, 1995; d'Acapito *et al.*, 2003; Boscherini, 2015) with very high surface sensitivity. As a grazing technique, the information depth is very low, often of the order of 1–10 nm, so this is a very strong and local surface probe of the density of states.

A variant of this with similar features is the total external XAFS or the X-ray standing wave (XSW) technique, where $90^\circ - \theta_{\rm inc} \simeq 2$–$7$ mrad $\simeq 0.1$–0.5°. Here, the X-ray wavefield is strongly confined to the surface as with ReflEXAFS. One should then use Fresnel equations and more complete electromagnetic theory to obtain information on the interaction of the spatial distribution of the wavefield in the material (Als-Nielsen & McMorrow, 2001). Information can be obtained about the spatial distribution of atoms normal to the surface by measuring the fluorescence as a function of the angle, which is the phenomenon and technique of X-ray standing waves. Analysis can be quite subtle, nonlinear and challenging to disentangle (Brown & Sturchio, 2002; Bedzyk & Cheng, 2002; Waychunas, 2002).

Alternate secondary modalities are dominated by radiationless relaxation, *i.e.* by Auger transitions.

7. Secondary processes: Auger transitions

Atomic inner-shell vacancy states tend to decay predominantly through radiationless or Auger transitions. These are auto-ionization processes arising from the Coulomb interaction between electrons. Radiationless transitions dominate over radiative transitions at low atomic number Z and also for $12 < Z < 30$ except for 1s vacancies in atoms, primarily because of the magnitude of the matrix elements and because far fewer channels are allowed by electric dipole X-ray emission selection rules than by the selection rules for Auger transitions (Chantler & Creagh, 2024). For example, 2784 electron–electron matrix elements can contribute to the radiationless decay of a $2p_{3/2}$ hole state in mercury (Crasemann, 1996).

Just like fluorescence and fluorescent XAFS detection, Auger electron emission can be considered as a two-step or higher-order process. The two-step process is valid if the ejected electron from photoionization is sufficiently energetic to not interact significantly with the Auger electron and the core-hole state interaction with the Auger continuum is weak. This is effectively the same comparison of timescales as discussed for the fluorescence process. The hole state then decays according to Fermi's golden rule. In the independent-electron central-field approximation, the nonrelativistic matrix element for a direct Auger transition can be given as

$$D = \left\langle n''l''j''(1);\, \varepsilon_{\rm a} l_{\rm a} j_{\rm a}(2) \right| \left| \frac{e^2}{\mathbf{r}_1 - \mathbf{r}_2} \right| \left| nlj(1) n'l'j'(2) \right\rangle, \qquad (15)$$

with the Auger electron labelled by quantum numbers $\varepsilon_{\rm a} l_{\rm a} j_{\rm a}$, the physically indistinguishable exchange Auger process given by

$$E = \left\langle n''l''j''(2);\, \varepsilon_{\rm a} l_{\rm a} j_{\rm a}(1) \right| \left| \frac{e^2}{\mathbf{r}_1 - \mathbf{r}_2} \right| \left| nlj(1) n'l'j'(2) \right\rangle \qquad (16)$$

and the transition probability per unit time given by $P_{\rm if} = (2\pi/\hbar)|D - E|^2 \rho(E_{\rm f})$, where $\rho(E_{\rm f})$ is the density of final states for the energy $E_{\rm f}$ satisfying the Fermi golden rule for energy conservation. The Auger process has an initial hole in $(n''l''j'')$, leading to two vacancies (nlj), $(n'l'j')$ and labelled as $(n''l''j'')$–$(nlj)(n'l'j')$ or, as examples, $K_{\rm I}$–$L_{\rm I}L_{\rm II}$ or $L_{\rm I}$–$M_{\rm II}M_{\rm III}$. For example, the KLL Auger process begins with a K-hole (from photoionization) being filled by an L-shell electron, with a second L-shell electron emitted into the continuum as an Auger electron, which can then be measured by Auger spectroscopy.

Coster–Kronig transitions are Auger transitions where the initial vacancy and one of the remaining vacancies are different subshells of the same shell, $L_{\rm I}$–$L_{\rm II}M_{\rm III}$, and are very fast because of large wavefunction overlap and low energies of the ejected electron, yielding hole widths in excess of 10 eV (lifetimes of $<10^{-16}$ s) for, for example, the $L_{\rm I}$ and $L_{\rm II}$ subshells at higher Z. McGuire coined the name super-Coster–Kronig transitions for the even faster type of Auger and Coster–Kronig transitions where both resulting vacancies are in the same shell as the initial vacancy, for example $M_{\rm I}$–$M_{\rm III}M_{\rm V}$ (McGuire, 1972).

8. Secondary processes: electron-yield measurements

Electron-yield detection is similar to fluorescence yield, measuring the decay products when the initial hole is filled. The path length is dependent upon the electron energy, but is typically of the order of 1000 Å, making the technique surface-sensitive. While self-absorption of photons is avoided, (self-) absorption of electrons causes the extreme surface sensitivity which can be used as a sensitive probe of surface processes, but much less so of bulk phenomena.

The sample is, in effect, inside the detector. In total electron yield (TEY), which is used for soft X-ray studies, the sample is under high vacuum and the electrons are collected by electrodes. At higher energies, conversion electron detection can be used, where emitted electrons collide with (helium) gas inside the detector, yielding an ionization chamber cascade, assuming that the sample can be made sufficiently conductive.

In principle, electron-yield measurements include Auger and photoionization and secondary electrons, including the

measurement of electrons from inelastic scattering. Energy resolution or separation of processes can be a challenge. Other methods for secondary process or decay product detection are possible, such as detection of visible light from the sample or X-ray excited optical luminescence (XEOL), but are useful largely in specialized cases. We now progress to give some basis for the choice of experimental and detection methods for a particular sample and a particular scientific question.

9. Selection of preferred detection modality

Figs. 2, 3, 4 and 5 illustrate traditional and current strengths for the analysis of long-range order (crystal symmetry, structure), medium-range order (tertiary structure of large molecules, molecular sizes, dimer separations *etc.*), which are normally investigated by alternate and complementary techniques, in particular crystallography, short/medium-range order of any phase, ordered or disordered, which is best addressed using the techniques in this chapter, and short-range order of surface properties (surface structure, plasmons, reflectivity *etc.*), which can be investigated using the techniques in this volume or by alternate methods. All such prescriptions are illustrative and are dominated by the specific scientific question to hand. They also should not be proscriptive. As scientists, we can find new truths in many unexpected areas. We categorize these choices of technique particularly to aid scientists learning or crossing over from alternate techniques.

For a solid, powder pellet or solution, one distinguishes the sample absorption or attenuation from the substrate (matrix, solvent) attenuation (see the definitions above).

Absorption (transmission) experiments normally follow the Nordfors criterion $2 < \ln(I_0/I) < 4$ or $10 < (I_0/I) < 100$, corresponding to $2 < [\mu/\rho][\rho t] < 4$ (Nordfors, 1960; Creagh & Hubbell, 1987, 1990). This was modified to recognize the

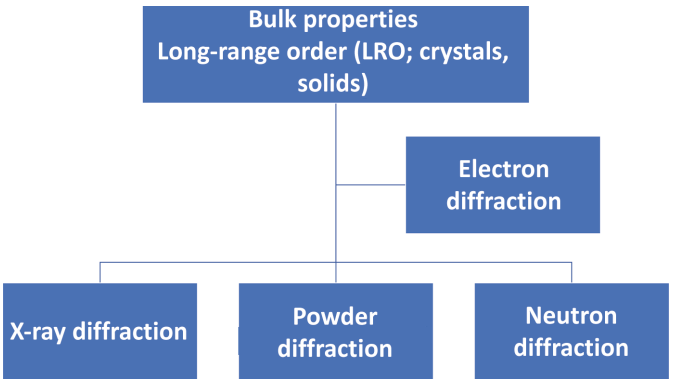

Figure 2
Selection of experimental modality based on sample form and scientific question. If the question relates to bulk properties (structure, space group, quasi-crystallinity, inelastic mean free path, bulk plasmons *etc.*) and the interest is in long-range order characteristics, then these techniques are exemplars and the reader should, for example, consult *International Tables for Crystallography* Volume C.

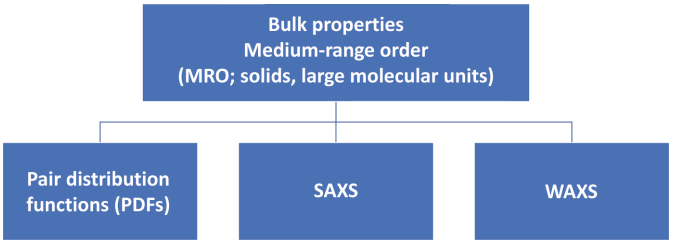

Figure 3
Selection of experimental modality based on sample form and scientific question. If the question relates to bulk properties (dimer or molecular subunit sizes and connectivity) and the interest is in medium-range order characteristics, then these techniques are exemplars and the reader should, for example, consult *International Tables for Crystallography* Volume H.

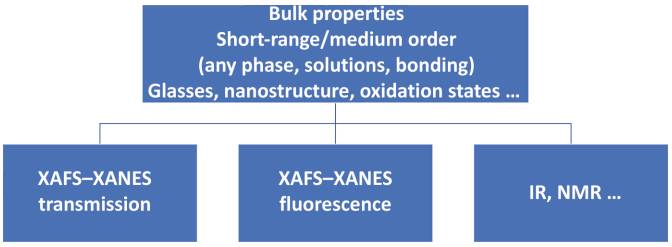

Figure 4
Selection of experimental modality based on sample form and scientific question. If the question relates to bulk properties (structure, bonding, disordered systems) and the interest is in short- or medium-range order characteristics, then these techniques are exemplars and the reader should consult this volume. IR and NMR are discussed elsewhere and under complementary techniques. The selection of XANES or XAFS and transmission or fluorescence is discussed in this chapter.

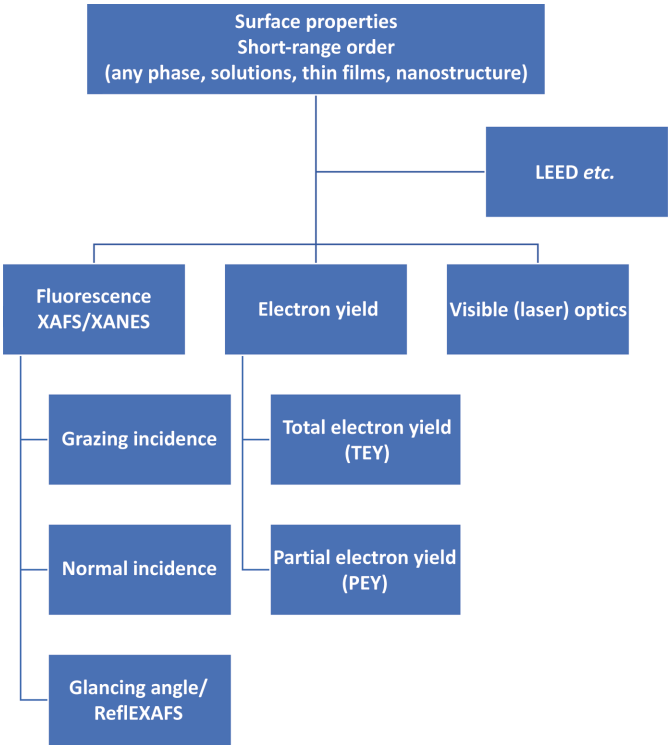

Figure 5
Selection of experimental modality based on sample form and scientific question. Specialized surface techniques for short-range order. Fluorescence and electron-yield modalities are discussed in this chapter and extensively in later chapters; laser optics and LEED *etc.* are discussed elsewhere.

Table 2
Constraints on detection modalities: general considerations.

Modality	Primary requirement	Secondary recommendations	Typical samples
Transmission	$0.5 < \ln(I_0/I) < 6$, $1.7 < (I_0/I) < 1000$ **Bulk** properties, $0.5 < [\mu/\rho][\rho t] < 6$ Measure dead time, dark current, blank	Nordfors; above and below edge Multiple thicknesses, concentrations $[\mu/\rho]^*_{pe} > 0.1 \times [\mu/\rho]$	Foils, inorganics Concentrated solutions XAFS
Hybrid transmission	**Bulk** properties, $0.5 < [\mu/\rho][\rho t] < 6$ Measure solvent, matrix	$[\mu/\rho]^*_{pe} > 0.01 \times [\mu/\rho]$	>1 mM solutions >100 p.p.m. powders
Fluorescence	'Any' $[\mu/\rho][\rho t]$ $[\mu/\rho]^*_{pe} \leq 0.1 \times [\mu/\rho]$ **Bulk** properties, measure self-absorption	$[\mu/\rho][\rho t] \geq 6$ or $[\mu/\rho][\rho t] \leq 0.5$ Avoid strong Bragg diffraction	<10 mM <1000 p.p.m. XANES, pre-edge
Normal incidence fluorescence	**Surface** electronic density of states Note self-absorption is large	$\alpha \simeq \pi/2$, $\beta \simeq 1$–5°	$t_d \simeq 10$–100 nm Thin layers
Grazing-incidence fluorescence	**Surface** electronic density of states Note absorption is large	$\alpha \simeq 1$–5°, $\beta \simeq \pi/2$	$t_d \simeq 10$–100 nm Thin layers
ReflEXAFS	**Local surface** probe	$\alpha \simeq 0.1$–$0.5^\circ \simeq \beta$ $[\mu/\rho][\rho t] \geq 6$	$t_d \simeq 1$–10 nm Thin layers
Electron yield	**Surface**, in-vacuum measurement	Low-energy X-rays $[\mu/\rho][\rho t] \geq 6$ and $[\mu/\rho]^*_{pe} > 0.1 \times [\mu/\rho]$	$t_d \simeq 100$ nm Thin layers

statistical quality attainable with high statistical accuracy (Chantler *et al.*, 2001; Chantler, Barnea *et al.*, 2012), $0.5 < \ln(I_0/I) < 6$ or $1.7 < (I_0/I) < 1000$, corresponding to a constraint on the mass attenuation coefficient and sample thickness and density, $0.5 < [\mu/\rho][\rho t] < 6$. The limits of the range require less than five times the count rate or counting time to achieve the same (0.5%) statistical precision on the determination of the ratio (Fig. 6).

For XAS this must relate to the attenuation above the edge, but it is important for pre-edge analysis that it is valid below the edge. Often, this is most easily accomplished with two independent samples and thicknesses. To achieve high accuracy with respect to common systematics, one should regularly measure dead time, dark current, blank samples and multiple thicknesses or concentrations.

We may consider a statistical precision limit on the edge jump to be similarly defined as $[\mu/\rho]^*_{pe} > 0.1 \times [\mu/\rho]$, to be conservative, so that the fraction of the absorption relating to the edge is at least 10% or so that the edge jump/total attenuation > 10%. The flux requirement to attain a statistical measurement on the edge step is then no worse than 100× that for the measurement of the full absorption coefficient (Table 2). However, this rule is beamline-dependent, according to the photon flux density on the target. Clearly, the statistical precision of the XANES and XAFS will be weaker than the precision on the edge jump, but the counting time can always increase accordingly.

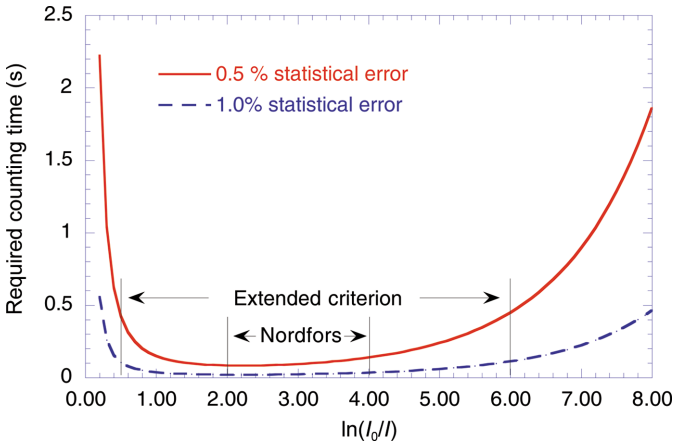

Figure 6
Traditional Nordfors criterion for attenuation using typical ion-chamber attenuation, for example above the edge (or below), illustrating the small cost of statistical precision in the determination of the ratio across the extended Nordfors range, as discussed in the text.

If the measurement follows the hybrid transmission technique, which is particularly designed for high-accuracy data collection from dilute samples, then the matrix, solvent or cell is measured separately and it is perfectly feasible to have $[\mu/\rho]^*_{pe} > 0.01 \times [\mu/\rho]$. This has been proven with 15 mM or 1000 p.p.m. solutions, where, for example, edge jump/total attenuation $\simeq 3\%$ or $[\mu/\rho]^*_{pe} > 0.03 \times [\mu/\rho]$ (Chantler *et al.*, 2015; Islam *et al.*, 2016), and also works to produce a good χ spectrum at 1.5 mM or 100 p.p.m., or edge jump/total attenuation $\simeq 0.3\%$ or $[\mu/\rho]^*_{pe} > 0.003 \times [\mu/\rho]$. The use of a reference blank cell with solvent becomes critical here in order to minimize statistical noise in the extracted measurement. This could correspond to a counting time some 10^4 times that of an ideal metal foil, but such concentrations are often the case, and excellent spectra and accuracy can be obtained with bending-magnet beamlines under normal conditions. Often the range of good-quality measurements extends across a more limited but nonetheless very useful k-range. The effective k-range is beamline-dependent, but these estimates are based on a simple bending-magnet beamline. The limits from statistical precision or from systematics have not yet been determined; see also Best & Chantler (2024).

On the assumption that the insight and structure from fluorescence spectra are the same or equivalent to those from absorption (see above and, for example, Trevorah *et al.*, 2019), some beamline staff would caution against too concentrated a sample for fluorescence measurements, for example for single-crystal systems, especially of silicon or ideal structures which may have very strong Bragg diffraction into the fluorescence detector. Many fluorescence detectors can cope with this direct diffraction peak. However, a concentration such as this will indicate a preference for and higher statistical quality

from transmission rather than fluorescence. At some point which remains unclear, if attenuation is too high or if attenuation is too low, or if the edge jump is too small a fraction of the attenuation, then fluorescence is indicated. So, for example, one could estimate that fluorescence is particularly useful if $[\mu/\rho][\rho t] \geq 4$ (on the basis that the sample is becoming too thick for a transmission measurement, but fluorescence may be able to yield a clean background) or $[\mu/\rho][\rho t] \leq 0.5$ (the sample may be becoming too thin for a transmission measurement, but fluorescence may be able to yield a clean background) or edge jump/total attenuation of $\leq$5–10% or $[\mu/\rho]^{*}_{\rm pe} \leq 0.05 \times [\mu/\rho]$ (where transmission may observe a large background from matrix or solvent, which is absent in fluorescence measurement).

Self-absorption is large when $[\mu_{\rm f}/\rho]$ is large and absorption is large when $[\mu/\rho]$ is large, and these can be dominant distortions of the signal if self-absorption is not corrected for (Trevorah *et al.*, 2019). If these are corrected for, then the applicability of fluorescence is convenient and valuable across wide ranges of investigation.

Normal incidence fluorescence, $\alpha \simeq \pi/2$, $\beta \simeq 1$–5°, is indicated for studies of the surface electronic density of states rather than bulk measurements. Self-absorption is large and the information depth $t_{\rm d} \simeq$ 10–100 nm. In principle, this can characterize sample, detection geometry, pixel size and sample roughness.

Grazing-incidence fluorescence, $\alpha \simeq 1$–5°, $\beta \simeq \pi/2$, is also indicated for studies of the surface density of states rather than bulk measurements. Absorption is large, the spectrum is distorted and the information depth $t_{\rm d} \simeq$ 10–100 nm.

Glancing-angle fluorescence or ReflEXAFS, $\alpha \simeq 0.1$–$0.5^{\circ} \simeq \beta$, dominated by reflection coefficients but with a transformed XAFS structure, is indicated for strong and local studies of the surface density of states rather than bulk measurements. Absorption is large, the spectrum is distorted and the information depth is very short: $t_{\rm d} \simeq$ 1–10 nm. This is almost a pure surface technique and can separate the surface plasmons, for example.

Total electron yield, as opposed to the above, requires in-vacuum measurements and is mainly suitable for soft X-rays and towards vacuum UV energies, perhaps $E < 3$ keV. This becomes more useful especially where the attenuation of the X-rays and the self-absorption is far too high. The electrons likewise are attenuated, so it is a surface probe, with an information depth of the order of $t_{\rm d} \simeq 100$ nm. This is useful when the absorption is very high (soft X-rays) and the self-absorption is very high (soft X-rays) and a surface probe is desired.

A more careful study of the comparative speed or accuracy of transmission, fluorescence and other modalities requires real exemplars, some of which will be given in the experimental chapters in this volume.

10. Links

This chapter gives an overview of the physical processes of secondary modalities and comparisons between them; however, it does not give real-world examples of comparisons in practice, or of detailed theoretical computations, which are in part the subjects of other experimental and theoretical chapters in this volume. Theory is introduced in the early chapters (Chantler & Creagh, 2024; Paolasini & Di Matteo, 2024; Natoli *et al.*, 2024; de Groot, 2024; Fujikawa, 2024; Rehr *et al.*, 2024), which applies to all modalities but especially to transmission XAFS. It is emphasized that XANES fingerprinting may yield different qualitative information for transmission and fluorescence modalities (Fujikawa, 2024) and that pre-edge structure should in general be investigated by transmission (Yamamoto, 2024). Most of the subsequent theory chapters apply equally well to fluorescence and transmission. Specific scattering experiments, of which fluorescence is a subset of inelastic scattering modalities, are discussed in Glatzel *et al.* (2024), Renevier & Proietti (2024*a*) and Sham (2024). The combination of modalities for complementary insight is discussed in Best (2024) and Castellano (2024). Additional topics generally relevant for all modalities and a series of well developed applications are discussed in Röhlsberger & Hu (2024).

Chantler & Bourke (2024) provide key tables and compilations of useful data to enable theoretical or computation work on fluorescence, transmission and other modalities. In particular, fluorescence yields f (total, partial, K shell, $L_{\rm I}$ shell *etc.*) are discussed and tabulated in Chantler & Bourke (2024), $K\alpha$ and $K\beta$ fluorescent component energies are discussed and tabulated in Chantler *et al.* (2024), $K\alpha_2/K\alpha_1$ and $K\beta/K\alpha$ integrated area or intensity ratios are provided in Chantler & Bourke (2024), edge or hole widths and edge lifetimes are also discussed in Chantler & Bourke (2024) and inelastic mean free paths of the photoelectron are tabulated and discussed in Chantler & Bourke (2024).

Chapters that particularly expand on fluorescence issues include Best & Chantler (2024) on hybrid techniques and self-absorption and Woicik & Pianetta (2024), d'Acapito (2024*a*), van der Laan (2024) and Renevier & Proietti (2024*b*) on detailing the secondary modalities. Self-absorption is also dealt with in Bridges & Booth (2024), while experimental aspects of RIXS are dealt with in Glatzel & Ghiringhelli (2024). Data collection in grazing incidence is discussed in d'Acapito (2024*b*). A later part of this volume provides many types of applications of transmission and fluorescence detection in major fields.

11. Conclusion and future perspectives

These additional chapters detail many of the future perspectives of fluorescent and secondary modalities. One of the most exciting areas is the issue of information content and insight, the statistical quality and type and range of information from one modality versus another, and the sensitivity of probes of polarization, wavevector, scattering angle, RIXS and others. While these are often difficult to investigate on standard beamlines, the future potential is enormous, and clear elucidation of the complementary insight from, for example, K-edge structure versus $L_{\rm II/III}$-edge structure in transmission,

and of XANES versus XAFS, or fluorescence signal versus transmission, will remain very valuable into the future. Again, the potential for a technique to be sensitive to a range of k, a range of nearest neighbours and a range of depth, to be sensitive to surface and bulk properties, and to distinguish between them, will be a developing and continuing opportunity.

References

Als-Nielsen, J. & McMorrow, D. (2001). *Elements of Modern X-ray Physics.* Chichester: John Wiley & Sons.

Barchewitz, R., Cremonese-Visicato, M. & Onori, G. (1978). *J. Phys. C Solid State Phys.* **11**, 4439–4445.

Bedzyk, M. J. & Cheng, L. (2002). *Rev. Mineral. Geochem.* **49**, 221–266.

Best, S. P. (2024). *Int. Tables Crystallogr. I*, ch. 2.22, 205–216.

Best, S. P. & Chantler, C. T. (2024). *Int. Tables Crystallogr. I*, ch. 3.14, 375–394.

Booth, C. H. & Bridges, F. (2005). *Phys. Scr.* **2005**, 202.

Borthen, P. & Strehblow, H.-H. (1995). *Phys. Rev. B*, **52**, 3017–3019.

Boscherini, F. (2015). *X-ray Absorption Spectroscopy of Semiconductors*, edited by C. S. Schnohr & M. C. Ridgway, p. 77. Berlin, Heidelberg: Springer.

Bridges, F. & Booth, C. H. (2024). *Int. Tables Crystallogr. I*, ch. 3.44, 564–566.

Brown, G. E. J. & Sturchio, N. C. (2002). *Rev. Mineral. Geochem.* **49**, 1–115.

Bunker, G. (2010). *Introduction to XAFS: A Practical Guide to X-ray Absorption Fine Structure Spectroscopy.* Cambridge University Press.

Castellano, C. (2024). *Int. Tables Crystallogr. I*, ch. 2.23, 217–224.

Chantler, C. T., Barnea, Z., Tran, C. Q., Rae, N. A. & de Jonge, M. D. (2012). *J. Synchrotron Rad.* **19**, 851–862.

Chantler, C. T. & Bourke, J. D. (2024). *Int. Tables Crystallogr. I*, ch. 2.25, 230–269.

Chantler, C. T. & Creagh, D. C. (2024). *Int. Tables Crystallogr. I*, ch. 2.1, 21–40.

Chantler, C. T., Islam, M. T., Best, S. P., Tantau, L. J., Tran, C. Q., Cheah, M. H. & Payne, A. T. (2015). *J. Synchrotron Rad.* **22**, 1008–1021.

Chantler, C. T., Rae, N. A., Islam, M. T., Best, S. P., Yeo, J., Smale, L. F., Hester, J., Mohammadi, N. & Wang, F. (2012). *J. Synchrotron Rad.* **19**, 145–158.

Chantler, C. T., Smale, L. F. & Hudson, L. T. (2024). *Int. Tables Crystallogr. C*. In the press.

Chantler, C. T., Tran, C. Q., Barnea, Z., Paterson, D., Cookson, D. J. & Balaic, D. X. (2001). *Phys. Rev. A*, **64**, 062506.

Chen, H. & Heald, S. M. (1993). *J. Appl. Phys.* **73**, 2467–2471.

Crasemann, B. (1996). *Atomic, Molecular and Optical Physics Handbook*, edited by G. W. F. Drake, pp. 701–711. New York: AIP.

Creagh, D. C. & Hubbell, J. H. (1987). *Acta Cryst.* A**43**, 102–112.

Creagh, D. C. & Hubbell, J. H. (1990). *Acta Cryst.* A**46**, 402–408.

d'Acapito, F. (2024*a*). *Int. Tables Crystallogr. I*, ch. 4.5, 613–616.

d'Acapito, F. (2024*b*). *Int. Tables Crystallogr. I*, ch. 3.32, 504–507.

d'Acapito, F., Davoli, I., Ghigna, P. & Mobilio, S. (2003). *J. Synchrotron Rad.* **10**, 260–264.

Eisebitt, S., Böske, T., Rubensson, J. & Eberhardt, W. (1993). *Phys. Rev. B*, **47**, 14103–14109.

Frenkel, A. I., Pease, D. M., Budnick, J. I., Shanthakumar, P. & Huang, T. (2007). *J. Synchrotron Rad.* **14**, 272–275.

Fujikawa, T. (2024). *Int. Tables Crystallogr. I*, ch. 2.5, 60–70.

Glatzel, P. & Ghiringhelli, G. (2024). *Int. Tables Crystallogr. I*, ch. 3.49, 586–591.

Glatzel, P., Juhin, A. & Moretti, M. (2024). *Int. Tables Crystallogr. I*, ch. 2.19, 177–189.

Goulon, J., Goulon-Ginet, C., Cortes, R. & Dubois, J. M. (1982). *J. Phys. Fr.* **43**, 539–548.

Groot, F. de (2024). *Int. Tables Crystallogr. I*, ch. 2.4, 55–59.

Heald, S. M., Chen, H. & Tranquada, J. M. (1988). *Phys. Rev. B*, **38**, 1016–1026.

Islam, M. T., Best, S. P., Bourke, J. D., Tantau, L. J., Tran, C. Q., Wang, F. & Chantler, C. T. (2016). *J. Phys. Chem. C*, **120**, 9399–9418.

Jaklevic, J., Kirby, J. A., Klein, M. P., Robertson, A. S., Brown, G. S. & Eisenberger, P. (1977). *Solid State Commun.* **23**, 679–682.

Jaklevic, J., Kirby, J. A., Klein, M. P., Robertson, A. S., Brown, G. S. & Eisenberger, P. (1993). *Solid State Commun.* **88**, 1105–1108.

Joly, Y. & Grenier, S. (2016). *X-ray Absorption and X-ray Emission Spectroscopy*, edited by J. A. Bokhoven & C. Lamberti, pp. 73–97. Chichester: John Wiley & Sons.

Laan, G. van der (2024). *Int. Tables Crystallogr. I*, ch. 3.33, 508–515.

Lee, P. A., Citrin, P. H., Eisenberger, P. & Kincaid, B. M. (1981). *Rev. Mod. Phys.* **53**, 769–806.

Martens, G. & Rabe, P. (1980). *Phys. Status Solidi A*, **58**, 415–424.

McGuire, E. J. (1972). *Phys. Rev. A*, **5**, 1043–1047.

Natoli, C. R., Hatada, K. & Sébilleau, D. (2024). *Int. Tables Crystallogr. I*, ch. 2.3, 48–54.

Newville, M. (2014). *Rev. Mineral. Geochem.* **78**, 33–74.

Nordfors, B. (1960). *Ark. Fys.* **18**, 37–47.

Paolasini, L. & Di Matteo, S. (2024). *Int. Tables Crystallogr. I*, ch. 2.2, 41–47.

Parratt, L. G. (1954). *Phys. Rev.* **95**, 359–369.

Pease, D. M., Brewe, D. L., Tan, Z., Budnick, J. I. & Law, C. C. (1989). *Phys. Lett. A*, **138**, 230–234.

Pfalzer, P., Urbach, J.-P., Klemm, M., Horn, S., denBoer, M., Frenkel, A. & Kirkland, J. (1999). *Phys. Rev. B*, **60**, 9335–9339.

Rehr, J. J., Kas, J. J. & Vila, F. D. (2024). *Int. Tables Crystallogr. I*, ch. 2.6, 71–79.

Renevier, H. & Proietti, M. G. (2024*a*). *Int. Tables Crystallogr. I*, ch. 2.21, 201–204.

Renevier, H. & Proietti, M. G. (2024*b*). *Int. Tables Crystallogr. I*, ch. 3.34, 516–519.

Röhlsberger, R. & Hu, M. Y. (2024). *Int. Tables Crystallogr. I*, ch. 2.24, 225–229.

Sham, T. K. (2024). *Int. Tables Crystallogr. I*, ch. 2.20, 190–200.

Trevorah, R. M., Chantler, C. T. & Schalken, M. J. (2019). *IUCrJ*, **6**, 586–602.

Tröger, L., Arvanitis, D., Baberschke, K., Michaelis, H., Grimm, U. & Zschech, E. (1992). *Phys. Rev. B*, **46**, 3283–3289.

Waychunas, G. (2002). *Rev. Mineral. Geochem.* **49**, 267–315.

Woicik, J. C. & Pianetta, P. (2024). *Int. Tables Crystallogr. I*, ch. 3.31, 500–503.

Yamamoto, T. (2024). *Int. Tables Crystallogr. I*, ch. 2.7, 80–87.

Zschech, E., Tröger, L., Arvanitis, D., Michaelis, H., Grimm, U. & Baberschke, K. (1992). *Solid State Commun.* **82**, 1–5.